ACSNANO

www.acsnano.org

ARTICLE

Millisecond Conversion of Metastable 2D Materials by Flash Joule Heating

Weiyin Chen, Zhe Wang, Ksenia V. Bets, Duy Xuan Luong, Muqing Ren, Michael G. Stanford, Emily A. McHugh, Wala A. Algozeeb, Hua Guo, Guanhui Gao, Bing Deng, Jinhang Chen, John Tianci Li, William T. Carsten, Boris I. Yakobson,* and James M. Tour*

Cite This: *ACS Nano* 2021, 15, 1282−1290

Read Online

ACCESS | Metrics & More | Article Recommendations | Supporting Information

ABSTRACT: Controllable phase engineering is vital for precisely tailoring material properties since different phase structures have various electronic states and atomic arrangements. Rapid synthesis of thermodynamically metastable materials, especially two-dimensional metastable materials, with high efficiency and low cost remains a large challenge. Here we report flash Joule heating (FJH) as an electrothermal method to achieve the bulk conversion of transition metal dichalcogenides, MoS_2 and WS_2, from 2H phases to 1T phases in milliseconds. The conversions can reach up to 76% of flash MoS_2 using tungsten powder as conductive additive. Different degrees of phase conversion can be realized by controlling the FJH conditions, such as reaction duration and additives, which allows the study of ratio-dependent properties. First-principles calculations confirm that structural processes associated with the FJH, such as vacancy formation and charge accumulation, result in stabilization of the 1T phases. FJH offers rapid access to bulk quantities of the hitherto hard-to-access 1T phases, a promising method for further fundamental research and diverse applications of metastable phases.

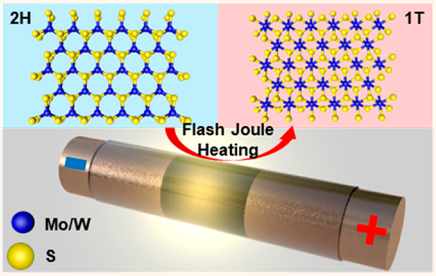

KEYWORDS: *flash Joule heating, phase engineering, metastable, 2D materials, transition metal dichalcogenide, phase conversion*

Recent research has shown that, in addition to the material components and dimensionality,[1−5] the arrangement of atoms within materials can greatly affect their chemical properties.[6−10] A common example is the variety of transition metal dichalcogenide (TMD) materials. Composed of transition metals (M) from group IV_B to X_B and chalcogens (X), such as S, Se, and Te, TMD materials have a sandwich-like structure with the chemical formula MX_2.[2] For each TMD material, there are two distinguishable phases (Figure 1): the 1T phase, in which the M is octahedrally coordinated and belongs to the space group $P\bar{3}m$ (aBc arrangement, here lowercase and uppercase refer to the arrangement of X and M, respectively); and the 2H phase, in which M has trigonal prismatic coordination and belongs to the space group $P6_3/mmc$ (aBa arrangement).[4,11] The intrinsic electrical and optical properties of 1T and 2H phases are disparate, which broadens the applications of TMD materials at wider fields.[3,4,7−9] However, the formation energy difference between these two phases makes it difficult for the synthesis and application of the metastable counterparts.

For instance, two-dimensional (2D) MoS_2 and WS_2 are typical polymorphic materials in the family of TMD materials. The 2H phases are semiconductors, while the 1T phases have metallic properties.[12,13] The 2H phases are reported to be useful in sensing and electrical devices such as field effect transistors (FETs),[3,14] and the 1T phases have shown utility as electrocatalysts and in energy storage devices.[15−18] However, these 1T phases have a higher formation energy and are not stable in ambient conditions.[19,20] The Fermi surface nesting drives the 1T phase relaxation to reform 2H space groups by gliding one of the S planes in the ⟨210⟩ direction by $a/\sqrt{3}$ (a is the edge length in hexagonal lattice).[7] As a consequence, the direct synthesis of the metastable 1T phases is complicated. Although the postgrowth strategy of using ions to weaken the interaction between layers and induce the formation of metastable forms, such as 1T MoS_2, is well-known,[21,22] the cumbersome procedures and the introduction of various ions such as Li^+ limit wider-scale applications of these metastable materials. Additionally, it is reported that local cation-intercalation within the tetrahedral interstices will inevitably disrupt the S−Mo−S lattice framework and lead to in-plane structural fracture and crystal decomposition.[21] Thus, it would

Received: October 9, 2020
Accepted: December 14, 2020
Published: January 7, 2021

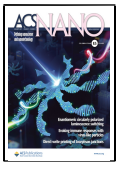

be beneficial to develop a one-step method to achieve these metastable forms with high efficiency and crystallinity.

Previous research has shown that, by applying an extremely high energy source, such as plasma induction or laser radiation, top chalcogen rows are observed being transversally displaced on the surface layer, which indicated local phase transition via these surface treatment strategies.[14,23] These local phase transitions are initiated or stabilized by the formation of chalcogen vacancies and achieved by different energy sources. Some of them, such as Ar-plasma, rely on the kinetic energies of ions, which are enough to break the S−Mo bonds and induce lateral sliding of top S-layer, but below the level to cause obvious etching effect.[14] Therefore, they are suitable for monolayer treatment. Other methods, such as laser radiation, depending on the focused laser with high local energy density, can cause continuous thinning to the flakes during laser irradiation.[23] Thus, they are suitable for flakes or multilayers (7∼30 layers). Here we have realized that flash Joule heating (FJH), which provides short electrical pulses of high energy density followed by rapid cooling,[24−29] can induce the bulk conversion of 2H phase MoS_2 and WS_2 to their respective 1T phases. Phase conversion to the metastable 1T phases is attributed to vacancy formation and negative charge accumulation to lower the formation energy of 1T phases, as shown by our theoretical calculations. During the FJH process, the current can reach >1350 A in 0.25 ms and the enormous electrical energy reaches 1.13×10^6 J mol^{-1}, which is ∼10 times more than the required activation energy for phase transition. In addition, we achieve different degrees of phase conversions by controlling the FJH conditions, such as reaction duration and additives, which allows the systematic study of ratio-dependent properties. FJH allows the use of bulk materials as reactants and has the potential for rapid access to bulk quantities of metastable phases to enrich the properties of materials and extend their applications.

RESULTS AND DISCUSSION

To prove the feasibility of FJH for inducing phase transitions, commercial MoS_2 or WS_2 powders were used as reactants. The reactants were slightly compressed inside a quartz or ceramic tube between two electrodes as shown in Figure 1. In order to increase the conductivity of the reactants, carbon black (5 wt %) was added and mixed evenly before the FJH reaction. A mild vacuum (∼10 mmHg) was applied to the system to limit sample oxidation and facilitate reaction outgassing. A high voltage electric discharge was applied by capacitor banks to convert MoS_2 or WS_2 from the 2H phase into the 1T phase within milliseconds. The products after the reactions are called flash MoS_2 or WS_2 in this context. Additional experimental details and a circuit diagram of the FJH setup can be found in the Experimental Section and Figure S1.

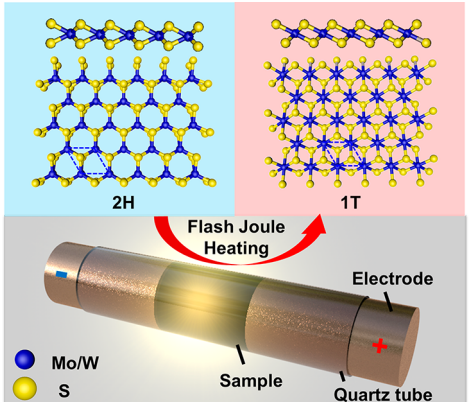

Figure 1. Schematic diagram of the phase conversion via FJH. The inset shows the atomic structure of the 2H and 1T phases from the side and top view.

From scanning electron microscopy (SEM), the morphology of flash MoS_2 is similar to that of reactant MoS_2 (Figure S2) and the particle size is 2−5 μm (Figure 2a). In the transmission electron microscopy (TEM) analyses (Figures 2b, S3, and S4), clear lattice fringes are observed, which infers high crystallinity of flash MoS_2. The number of layers in most regions is 1−8, and the average interlayer distance is ∼0.65 nm, which is ∼5% larger than 0.62 nm in intrinsic 2H MoS_2[16] and suggests efficient dispersibility in ethanol solutions (Figure S3). The UV−vis spectrum of a flash MoS_2 suspension shows a monotonic decrease of the absorbance with increasing wavelength (Figure S5), indicating the characteristics of a metallic nanostructure.[13] The thermal gravimetric analysis-differential scanning calorimetry (TGA-DSC) curve of flash MoS_2 (Figure S6) further shows a broad exothermic peak centered at ∼215 °C, which is related to the gradual phase transformation from the 1T phase to the 2H phase, indicating the metastable feature of 1T phases. The selected-area electron diffraction (SAED) results of the flash MoS_2 basal plane in different regions show a set of 6-fold diffraction patterns along the [001] zone axis (Figures 2c and S7), which excludes the existence of polycrystalline nanosheets with different orientations after the flash reaction. It has been reported that, along the [001] zone axis, the SAED patterns of 1T MoS_2 are the same as those of 2H MoS_2 in in-plane heterostructures, where the 1T phase is squeezed by the 2H counterparts.[30,31] The existence of the 1T phase in flash MoS_2 was further confirmed by atomic arrangement analysis with high angle annular dark-field scanning TEM (HAADF-STEM). The main difference between the 1T and 2H phases is that sulfur atoms above and below the molybdenum atom layers occupy overlapped positions in the [002] direction of the 2H phase but are evenly distributed in a tetrahedral vertex of the 1T phase[4,17,32−34] (Figure 1). Thus, HAADF-STEM can be used

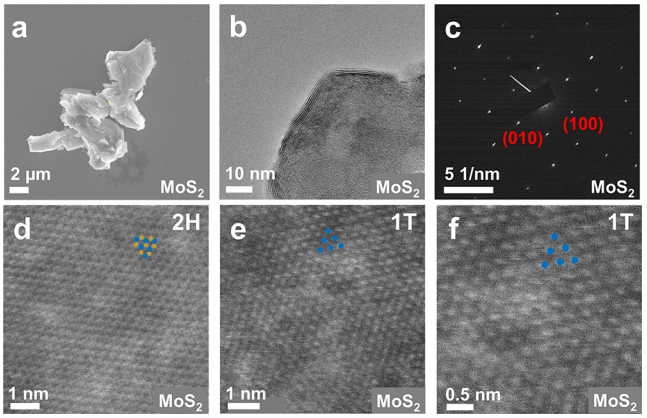

Figure 2. Characterization of morphology and atomic structure of flash MoS_2. (a) SEM image of flash MoS_2. (b) TEM image of flash MoS_2. (c) SAED pattern of flash MoS_2. (d−f) HAADF-STEM atomic images of flash MoS_2. Small lattice units are given to show 2H and 1T phases in the images (orange = S; blue = Mo).

https://dx.doi.org/10.1021/acsnano.0c08460
ACS Nano 2021, 15, 1282−1290

to characterize the atom positions and then differentiate the 1T and 2H regions (Figures 2d–f, S8, and S9). 2H MoS_2 with the honeycomb-like area and 1T MoS_2 with octahedral lattice is shown in Figure 2d and e, respectively. Figure 2f shows the 1T phase with higher magnification. To accentuate the atomic arrangements, small lattice units are shown in HAADF-STEM images (orange = S; blue = Mo). The intensity profiles of flash MoS_2 at different regions are plotted in Figure S8. The different arrangements of S atoms result in the intensity difference, which corresponds to distinguishable phases in the HAADF-STEM images.

In addition to flash MoS_2, the high-resolution TEM (HR-TEM) images of flash WS_2 are given in Figures 3a and S10.

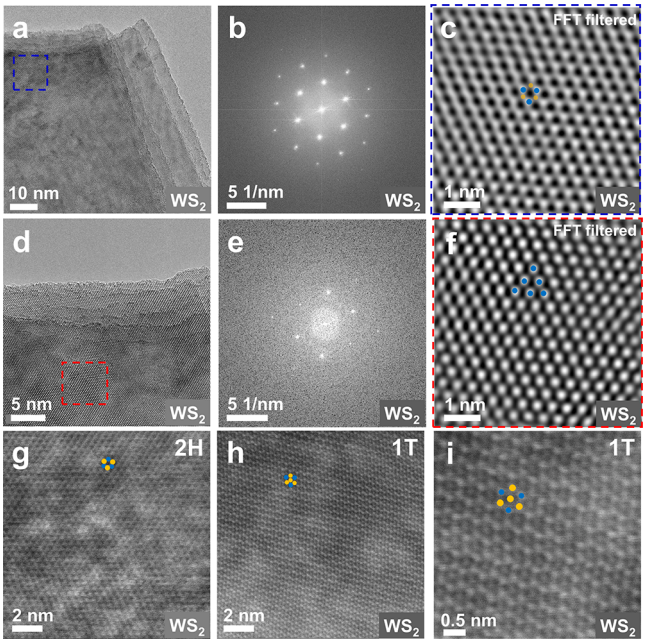

Figure 3. Atomic structure analysis of flash WS_2. (a) HR-TEM images of flash WS_2. (b) FFT of HR-TEM image in (a, blue boxed region). (c) FFT filtered image of (b). (d) HR-TEM images of flash WS_2. (e) FFT of HR-TEM image in (d, red boxed region). (f) FFT filtered image of (e). (g–i) HAADF-STEM atomic images of flash WS_2. Small lattice units are given to show the 2H and 1T phases in the images (orange = S; blue = W).

Individual large WS_2 sheets can be distinguished, and the sheet edges are not well aligned, which might be the result of the reduction of interlayer interaction. Figure 3b and e shows the fast Fourier transform (FFT) results from the blue and red boxed regions, respectively. Figure 3c and f displays the FFT filtered images of the corresponding regions. The blue boxed region shows a set of 6-fold diffraction patterns from the [002] direction and the intensity of each diffraction pattern is strong and equivalent, while the red boxed region shows similar 6-fold diffraction patterns with weaker signals. The nonequivalent {100} facets caused by the distorted structure result in the different intensities of diffraction patterns in Figure 3e.[35] Different lattice structures and their respective small crystal units (orange = S; blue = W) are shown in Figure 3c and f, which correspond to the 2H and 1T phase of flash WS_2. Atomic resolution HAADF-STEM images (Figures 3g–i and S11) clearly show the coexistence of 1T and 2H phases and small units are given in Figure 3g–i to show 2H and 1T phases (orange = S; blue = W).

The flash duration in the FJH process is an important variable for phase conversion (Figure 4). The ratios of 1T and 2H phase can be determined by X-ray photoelectron spectroscopy (XPS) analysis.[17,36] The Mo 3d peaks of 1T MoS_2 are located at 228.7 and 231.8 eV, corresponding to $3d_{5/2}$ and $3d_{3/2}$, respectively. The binding energies of the 1T phase for S $2p_{3/2}$ and S $2p_{1/2}$ are 161.8 and 162.9 eV, respectively. All of these peaks show a downfield shift of ~0.8 eV when compared to 2H MoS_2.[4] After deconvoluting the Mo and S peaks, the red and blue curves represent the 1T and 2H phases of MoS_2, respectively. Analysis of the XPS spectra for phase ratios and S/Mo ratios are reported in Figure 4d,e. As the reaction flash time increases, the average ratios of the 1T phase gradually become higher. The highest percentage of 1T MoS_2 reaches ~50% after a 300 ms flash treatment. Longer flash duration lowers the S/Mo ratios of the products and after 300 ms, the average S/Mo ratio is ~1.70. There are ~15% sulfur defects in the flash MoS_2 samples, which play an important role in making the phase boundary area less crowded and in stabilizing the 1T phase in the products.[37,38] However, longer flash duration also increases the mass loss and lowers the reaction yield of the mixed phase materials.

Raman spectroscopy plays a role in analytically confirming the existence of 1T MoS_2 based on the distinct phonon modes. For 2H MoS_2, two typical peaks at ~380 and 405 cm^{-1} are evident from E_{2g} (in-plane vibration of the two S atoms and Mo atom) and A_g mode (out of plane opposing vibration).[3] Because of the symmetry breaking in the trigonal lattice area, *J*-series peaks centered at 152 cm^{-1} (J_1, the out-of-plane motion of each row of Mo atoms within the zigzag chains and in-plane shearing vibration of a single row of Mo atoms relative to the other in a chain), 217 cm^{-1} (J_2, S atom layer shift with respect to Mo atom layers), and 335 cm^{-1} (J_3, breaking of each zigzag chain in 2 rows with a slight out-of-plane component)[8,39] can be clearly observed in 1T MoS_2. The representative Raman spectra (Figure 4c) and Raman mapping (Figure S12) confirm the existence of 1T MoS_2. As the reaction pulse time increases, the average ratio of J_3/E_{2g} generally increases as shown in Figure 4f, from which we can deduce that the ratio of 1T MoS_2 increases. This is consistent with the XPS results. X-ray diffraction (XRD) is an effective method to determine the material structure and lattice deformation.[13] In Figure S13, the XRD analyses of flash MoS_2 after different heating times are shown. Compared to 2H MoS_2, the intensity of the (002) peak in flash MoS_2 becomes weaker, which suggests that the layer number decreases after the FJH reaction. The position of (002) peak shifts from 14.4° (Powder Diffraction File 01-073-1508, 2H MoS_2) to 13.8° in FJH MoS_2, which means the interlayer distance expands from 0.62 to 0.65 nm, corresponding to the TEM results. The influence of carbon content in the reactant mixtures has also been investigated. The XPS and Raman spectra are shown in Figures S14 and S15. The ratios of carbon do not have an obvious effect on the 1T phase ratios on the flash MoS_2 samples. Similarly, the Raman and XPS analyses of flash WS_2 are shown in Figures S16 and S17. The characteristic *J*-series peaks of the 1T phase (J_1, ~130 cm^{-1}; J_2, ~184 cm^{-1}; and J_3, ~325 cm^{-1})[40] in flash WS_2 can be found (Figure S16), which infers the phase conversion of WS_2 during the FJH reaction. The W 4f peaks of 1T WS_2 locate at 32.7 and 34.7 eV corresponding to $4f_{7/2}$ and $4f_{5/2}$, respectively. The binding energies of the 1T phase for S $2p_{3/2}$ and S $2p_{1/2}$ are 162.0 and 163.2 eV, respectively (red curve, Figure S17).

https://dx.doi.org/10.1021/acsnano.0c08460
ACS Nano 2021, 15, 1282–1290

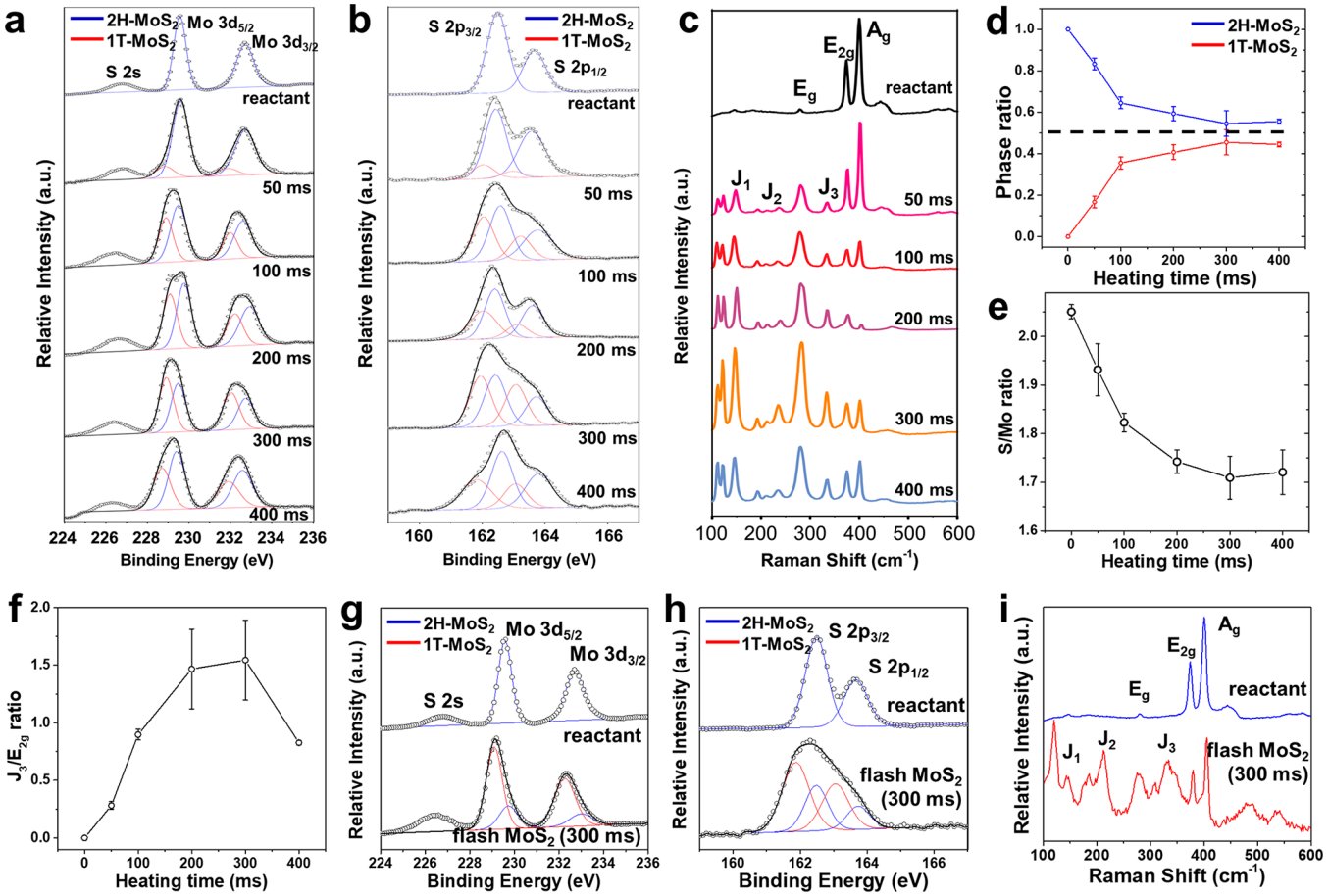

Figure 4. Effect of flash conditions on chemical components of flash MoS_2. (a,b) High resolution XPS of Mo 3d and S 2p spectra at various flash times from 50 to 400 ms. The red curve and blue curve represent the 1T and 2H phases of MoS_2, respectively. (c) Raman spectra of flash MoS_2 at different flash time. (d) Analysis of XPS spectra reporting the 1T and 2H phase ratios. (e) Analysis of XPS spectra reporting the S/Mo ratios. The error bars represent the standard deviation where the number of samples N is 3. (f) Ratio of J_3/E_{2g} at each flash time. The error bars represent the standard deviation where the number of samples N is 10. (g,h) High resolution XPS of flash MoS_2 sample using tungsten metal as conductive additive with optimized flash duration (300 ms). (g) Mo 3d spectra and (h) S 2p spectra. (i) Raman spectrum of flash MoS_2 made using tungsten metal as conductive additive with optimized flash duration (300 ms).

These peaks show a downfield shift of ~0.7 eV when compared to 2H WS_2 (blue curve, Figure S17).[17,41]

To further alter the 1T phase ratio after the FJH reaction, tungsten powder was used as the conductive additive in the reactant mixture. Compared to carbon black, tungsten has a lower electronegativity. The previous simulations have reported that negative charge doping can lower the formation energy of 1T MoS_2 and stabilize the metastable phase.[42] The tungsten additive can be the electron donor, alter the favorability of 1T phase and increase the maximum phase ratio. The XPS result of flash MoS_2 using tungsten powder as conductive additive reports a higher 1T ratio (~76%) as expected (Figure 4g,h). The J-series peaks are also found in flash MoS_2 using tungsten as the conductive additive, which infers the existence of 1T MoS_2 (Figure 4i). Similarly, the intensity of the (002) peak in flash MoS_2 made using tungsten as the conductive additive decreases (Figure S18), which indicates the layer number decreases after the FJH reaction and suggests efficient dispersibility in composites.

Using the first-principles density functional theory (DFT) calculations, we investigated the mechanism of the MoS_2 phase conversion during the FJH process. It is well-known that the 2H phase has a significantly lower structural energy (by ~0.8 eV per structural unit cell), resulting in thermodynamic preference and hence, high abundance in synthesis. During the FJH process, many structural changes, such as the formation of S vacancies indicated by the experimental observations as shown in Figure 4e, are enabled by a large amount of energy provided into the system (Figures S19 and S20). We considered the change in thermodynamic preference, characterized by the energy difference between two phases, due to the formation of the S monovacancies V_S and divacancies V_{S_2} (Figure 5). Positive values of the energy difference $\Delta E_{1T-2H} = E_{1T} - E_{2H}$ would correspond to the thermodynamic preference toward 2H phase, $\Delta E_{1T-2H} \approx 0$ indicates an equal probability of the phases, and negative values show a preference toward the 1T phase. Presuming the defects are uniformly dispersed throughout the large 8 × 8 hexagonal supercell, we found that an increase in the concentration of both V_S and V_{S_2} results in a significant decrease of ΔE_{1T-2H} and consequently a higher abundance of the 1T phase (see the Methods section for more details). We also studied the effects of the excessive negative charge that can accumulate due to the conditions during FJH. For simplicity, we used negative charge proportional to the sulfur deficiency of the material, considering V_S^- and V_S^{-6} (and $V_{S_2}^{-2}$ and $V_{S_2}^{-12}$ for divacancies). As was expected from the previous calculations,[43] negative

https://dx.doi.org/10.1021/acsnano.0c08460
ACS Nano 2021, 15, 1282−1290

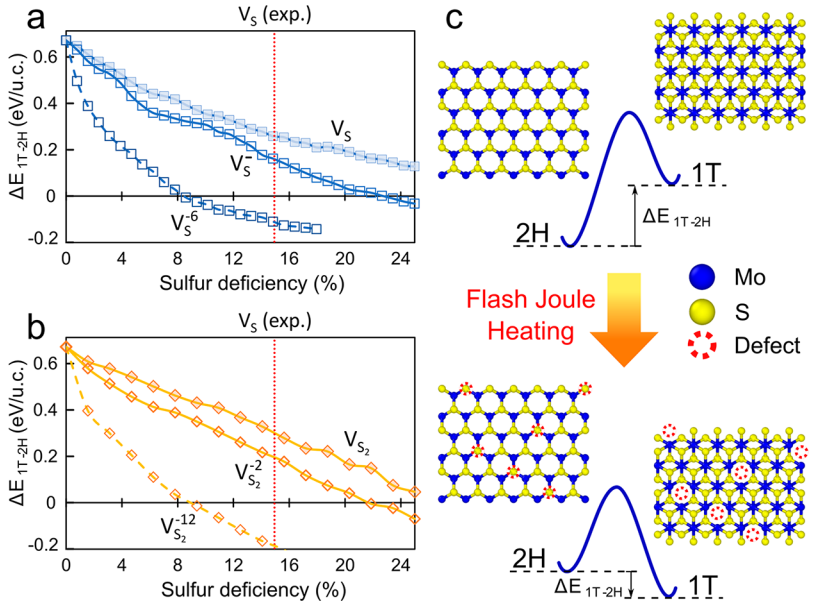

Figure 5. Energetics of the 1T phase stabilization through the formation of structural defects. Change of energy difference between 1T and 2H phases ΔE_{1T-2H} at various concentrations of neutral and negatively charged (a) single-vacancies and (b) divacancies. Note that the horizontal axis is chosen to be sulfur deficiency for the ease of comparison. An increase in the defect concentration, as well as excess negative charge, leads to a higher abundance of the 1T phase. An experimentally observed vacancy level is shown for reference. (c) Schematic diagram of the energy level before and after the FJH reaction.

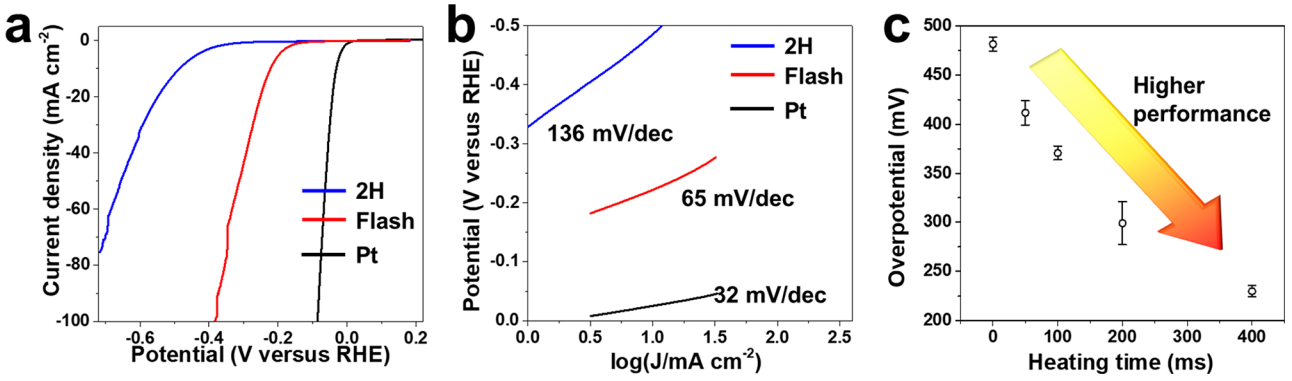

Figure 6. Exploration of ratio-dependent electrochemical performance. (a) Polarization curves and (b) corresponding Tafel plots of 2H MoS_2 and flash MoS_2 (400 ms flash duration). RHE, reversible hydrogen electrode. (c) The relationship between electrochemical overpotential at 10 mA cm^{-2} and reaction heating time. The error bars represent the standard deviation where N = 3.

charge stabilized the 1T phase allowing for negative ΔE_{1T-2H} even at relatively low defect concentration (less than 9% of V_S^{-6} leads to a thermodynamic preference toward the 1T phase, compared to ~15% observed experimentally). Finally, we considered the effect of the W addition in the FJH mixture, which experimentally was shown to increase the presence of the 1T phase by ~25% compared to the use of CB. In addition to increasing excessive charge accumulation that can be beneficial as was shown above, W can form substitutional defects W_{Mo}. We found that the presence of W_{Mo} did not affect the phase preference. However, if W indeed was partially incorporated into the MoS_2 lattice, it would effectively increase the sulfur deficiency of the material, leading to the increased preference toward the 1T phase.

The ratio-dependent properties of flash MoS_2 were further investigated via electrochemical hydrogen evolution reaction (HER). The formation of metallic 1T phase in flash MoS_2 is expected to tune the electronic structure and decrease the adsorption free energy of H* (ΔG_H^O), which can directly determine the energy barrier and reaction overpotential. A previous paper uncovered the existence of exposed active sites in the basal plane and hydrophilic properties of 1T−2H MoS_2 heterostructures, which can be controlled by changing the phase ratios.[44] The H_2 evolution potential at 10 mA cm^{-2} and Tafel slope of flash MoS_2 (400 ms flash duration) were measured to be −221 mV and 65 mV/dec, respectively, as shown in Figure 6a,b. The catalytic activity was improved compared to 2H MoS_2 powder (−491 mV and 136 mV/dec). As flash duration increased from 50 to 400 ms, the electrochemical overpotential decreased more than 250 mV (Figures 6c and S21), indicating a gradually improved catalytic activity and a strong ratio-dependent relationship.

CONCLUSION

In summary, the metastable 1T phases of MoS_2 and WS_2 are synthesized by FJH process within milliseconds. The obtained sheets show clear lattice fringes and diffraction patterns, confirming the high crystallinity of the flash samples.

https://dx.doi.org/10.1021/acsnano.0c08460
ACS Nano 2021, 15, 1282−1290

Compared to other strategies, such as the ion-assisted chemical vapor deposition, strong magnetic hydrothermal, or ion intercalated methods, FJH is fast, simple and can achieve the bulk conversion. First-principles DFT calculations reveal that the high current and large energy input result in the formation of structural defects such as S vacancies and the negative charge buildup leading to the thermodynamic preference toward the metastable 1T phase in FJH. Further, different degrees of phase conversions can be controllably achieved by FJH conditions, such as reaction durations and additives, which could lead to systematic study about ratio-dependent properties. More importantly, FJH offers the possibility of a promising method with high temperature and rapid cooling rate to synthesize bulk quantities of metastable materials, which is valuable for fundamental research and diverse applications.

METHODS

Materials. MoS_2 powder (average particle size (APS) 6 μm, 69860-100G) was purchased from Sigma-Aldrich. WS_2 powder (APS 2 μm, 243639-50G) was purchased from Sigma-Aldrich. Carbon black (CB, APS 10 nm, Black Pearls 2000) was purchased from Cabot Corporation. W metal powder (APS 1−5 μm, 99.9% metals basis) was purchased from Alfa Aesar. CB or W metal powder was used as conductive additives in the flash process. The FJH reactor setup was previously described.[24,28]

FJH System. The circuit diagram and FJH reaction box are shown in Figure S1. A quartz or ceramic tube is used to load the reactant powder; copper wool plugs or graphite spacers are utilized as electrodes to slightly compress the loaded powder. The powder is a mixture of WS_2 or MoS_2 powder with 5 wt % conductive additives. The conductive additives are CB or high melting point metal powders such as tungsten powder. Unless specified, the conductive additive in each reaction was 5 wt % CB. The reactants are mixed evenly to form the conductive mixture before being loaded into the tube. The compressing force is controlled by a small vise to tune the sample resistance to ∼1.6 kΩ. A mild vacuum (∼10 mmHg) is applied to the system by a sealed reaction chamber to avoid sample oxidation and facilitate reaction outgassing. An Arduino controller relay with programmable millisecond-level delay time is used to control the discharge time, and the electric energy is provided by a capacitor bank with a total capacitance of 60 mF. The capacitor bank is charged by a dc supply capable of reaching 400 V. Safety glasses designed for welding are generally suitable and recommended during the flash reaction because they effectively block infrared as well as ultraviolet light. For more safety notes and circuit design, our previous work has covered the comprehensive details.[24,28,29] A discharge voltage of 170 V was used at our experiment. After the FJH reaction, the apparatus was allowed to cool and vent for 5 min. For a quartz tube with 4 mm diameter and 5 cm length, an optimized sample weight is 80 mg of MoS_2 or 150 mg of WS_2. To achieve the highest 1T ratio in flash MoS_2 in our experiment, the reactant mixture is 80 mg of MoS_2 powder with 5 wt % tungsten powder. The flash conditions include 170 V discharge voltage with a total capacitance of 60 mF, 300 ms flash duration under a mild vacuum (∼10 mmHg).

Characterization. The reactant and flash products were characterized through SEM using a FEI Helios NanoLab 660 DualBeam scanning electron microscope at 5 kV with a working distance of 4 mm. TEM images and SAED patterns were taken with a JEOL 2100F field emission gun transmission electron microscope at 200 kV. Atomic resolution HR-TEM and HAADF-STEM images were taken with FEI Titan Themis S/TEM instrument at 80 keV after accurate spherical aberration correction. XPS data were collected with a PHI Quantera SXM Scanning X-ray Microprobe with a base pressure of 5×10^{-9} Torr. Survey spectra were recorded using 0.5 eV step sizes with a pass energy of 140 eV. Elemental spectra were recorded using 0.1 eV step sizes with a pass energy of 26 eV. All of the XPS spectra were corrected using the C 1s peaks (284.8 eV) as reference. Raman spectra were collected with a Renishaw Raman microscope using a 532 nm laser with a power of 5 mW. A 50× lens was used for local Raman spectra and Raman mapping. XRD measurements were done by a Rigaku SmartLab Intelligent XRD system with filtered Cu Kαradiation (λ = 1.5406 Å). UV−vis (Shimazu UV-3600 plus) was used to collect the spectra of the suspension of reactant and flash products. TGA was performed on a Mettler Toledo TGA/DSC 3+ system. TGA and DSC data were collected at a heating rate of 10 °C/min under air. The air flow was set to 80 mL/min.

HER Test. The slurry was prepared by dispersing 4 mg flash MoS_2 in 1 mL binder solution, which is 80 μL of 5 wt % Nafion solution mixed in 1 mL water/ethanol (1:1, volume ratio). The slurry was sonicated for 30 min to form a homogeneous ink. A volume of 12 μL of ink solution was loaded onto a glassy carbon electrode (3 mm in diameter) and dried in air at room temperature. The electrochemical measurements were carried out in a three-electrode configuration using a CHI 608D electrochemical workstation. A graphite rod and Hg/Hg_2SO_4, K_2SO_4 (saturated) electrode were used as the counter and reference electrodes, respectively. The electrolyte was 0.5 M H_2SO_4 sparged with Ar gas for Ar saturation. CV was carried out with potential ranging from 0.3 to −0.3 V (vs RHE) for 10 cycles at a scan rate of 50 mV s^{-1}. LSV was carried out with potential ranging from 0.2 to −0.8 V (vs RHE) at a scan rate of 5 mV s^{-1}.

Atomistic Ab Initio Calculations. Theoretical simulations were performed using first-principles density functional theory (DFT) calculations, as realized in the VASP software package. PAW potentials are employed for all species and the wave functions were expanded in a plane wave basis with energy cutoff of 400 eV. All calculations are spin-polarized and employ the Perdew−Burke−Ernzerhof (PBE) exchange-correlation functional. Spin−orbit coupling was included in all of the calculations.

For all calculations, we used an 8 × 8 hexagonal supercell with an additional 15 Å of vacuum included in the direction perpendicular to the MoS_2 surface to prevent interaction between periodic images (final supercell lattice parameters are a = 25.28 Å, c = 24 Å). Defects distribution ensuring the largest minimal distance between each pair of defects was used to provide uniform dispersion of vacancies within the material. For consideration of monovacancies, all defects were located within the same sulfur layer. The number of introduced vacancies was varied from 0 to 32 and 16 for mono- and divacancies respectfully, resulting in up to 25% sulfur deficiency in the system. An additional negative charge was introduced in the system through the alternation of the total number of electrons.

All structures underwent structural relaxation. The structures were relaxed until the forces on all atoms were less than 10^{-3} eV/Å, no additional constraints were imposed on the relaxation.

Analysis of the SAED Spectrum. A detailed calculation based on the SAED result in Figure S7 is shown as follows. In a reciprocal lattice, the distance $|\mathbf{b}_1|$ between {100} diffraction points and the center transmission point is 3.75 ± 0.11 nm^{-1} as shown in Figure S7. The axis vector $\mathbf{b}_1$ of the reciprocal lattice can be expressed as eq 1:

$$\boldsymbol{b}_1 = \frac{\boldsymbol{a}_2 \times \boldsymbol{a}_3}{\boldsymbol{a}_1 \cdot (\boldsymbol{a}_2 \times \boldsymbol{a}_3)} \tag{1}$$

$\mathbf{a}_1$, $\mathbf{a}_2$, and $\mathbf{a}_3$ are primitive vectors of the crystal lattice. Because MoS_2 belongs to hexagonal crystal system, $\mathbf{a}_1$ and $\mathbf{a}_2$ are perpendicular to $\mathbf{a}_3$, and the angle between $\mathbf{a}_1$ and $\mathbf{a}_2$ is $\frac{2\pi}{3}$. Thus, the relationship between $\mathbf{a}_1$ and $\mathbf{b}_1$ can be deduced as eq 2:

$$|\boldsymbol{b}_1| = \frac{1}{\left|\cos\frac{5\pi}{6}\right| \cdot |\boldsymbol{a}_1|} \tag{2}$$

The range of $|\boldsymbol{b}_1|$ is 3.64−3.86 nm^{-1}, and thus, the range of $|\boldsymbol{a}_1|$ is 0.299−0.317 nm.

$|\boldsymbol{b}_1|$ is larger than the value in 2H MoS_2 (3.56 nm^{-1})[5] and infers the slight lattice deformation caused by the phase transitions during the FJH reaction.

https://dx.doi.org/10.1021/acsnano.0c08460
ACS Nano 2021, 15, 1282−1290

Effect of Conductive Additives. Negative charge doping has been reported to be an effective method to achieve the phase conversion from 2H to 1T phase in MoS_2,[42] since a negative charge can lower the formation energy of 1T MoS_2 and stabilize the metastable phase. Compared to the C atom, the W atom has a lower electronegativity. Thus, the W powder additive can be the electron donor, alter the favorability of the 1T phase, and increase the maximum phase ratio. The other important advantage for using W powder is that the melting point of W is extremely high (>3400 °C) and thus W will not melt and aggregate together during the flash process. After the flash reaction with the optimized flash duration (300 ms), a higher percentage of 1T phase is obtained when W powder is used as conductive additive as shown in Figure 4g-i. After deconvoluting the Mo and S peaks, the red and blue curves represent the 1T and 2H phase of MoS_2, respectively (Figure 4g,h). The 1T phase percentage is 76%.

Energy Calculation of the FJH Reaction. The energy densities in Figure S19 are calculated based on the electrical energy input to the system. The energy barrier E_a for the 2H to 1T phase conversion is 1.3 eV, for energy unit with J g^{-1}, is shown in eq 3,

$$E_a = 1.3 \times 1.60 \times 10^{-19}\ \mathrm{J} \times N_A/M = 782.3\ \mathrm{J\ g^{-1}} \quad (3)$$

Here N_A is the Avogadro constant. For MoS_2, the molar mass M is 160.07 g mol^{-1}

The voltage input V_1 is 170 V and the total capacity C_{total} is 60 mF, and then input energy E_i can be calculated as in eq 4,

$$E_i = 0.5C_{total}(V_1^2 - V_2^2) = 567\ \mathrm{J} \quad (4)$$

V_2 is the voltage after FJH reaction.

For MoS_2, the mass of each batch m is 80 mg, so the energy that reactant absorbs per gram E is as in eq 5,

$$E = E_i/m = 7087.5\ \mathrm{J\ g^{-1}} \quad (5)$$

Thus, the input electrical energy is ~10 times the required activation energy. High input energy density is an important factor that induces some structural changes, such as the formation of S vacancies, which can trigger the phase conversion.

We can also estimate the input energy from the current profile (Figure S20). The electric work W_e is as in eq 6,

$$W_e = UIt = \int_{t_1}^{t_2} UI\ \mathrm{d}t = 540\ \mathrm{J} \quad (6)$$

Here, U is the average voltage for convenience. t_1 and t_2 are the starting and ending time, respectively, of the FJH reaction. Based on the above calculation, the input energy E_i can be used to estimate the electric work W_e to the samples during the reaction. And in Figure S20, the calculated energy densities are based on the input electrical energy by the capacitors. As shown in Figure 5a, after the FJH reaction, the energies of both the 1T phase (E_{1T}) and 2H phase (E_{2H}) decreased, and E_{1T} decreased more than E_{2H}. Thus, the energy difference $\Delta E_{1T-2H} = E_{1T} - E_{2H}$ becomes more negative after the reaction and the favorability of 1T phase can be altered.

ASSOCIATED CONTENT

Supporting Information

The Supporting Information is available free of charge at https://pubs.acs.org/doi/10.1021/acsnano.0c08460.

TEM, SEM, and other images; XPS and Raman spectra; additional graphs (PDF)

AUTHOR INFORMATION

Corresponding Authors

Boris I. Yakobson − *Department of Chemistry, Department of Materials Science and NanoEngineering, and Smalley-Curl Institute, Rice University, Houston, Texas 77005, United States*; Email: biy@rice.edu

James M. Tour − *Department of Chemistry, Department of Materials Science and NanoEngineering, Smalley-Curl Institute, NanoCarbon Center, the Welch Institute for Advanced Materials, and Smalley-Curl Institute, Rice University, Houston, Texas 77005, United States*; orcid.org/0000-0002-8479-9328; Email: tour@rice.edu

Authors

Weiyin Chen − *Department of Chemistry, Rice University, Houston, Texas 77005, United States*

Zhe Wang − *Department of Chemistry, Rice University, Houston, Texas 77005, United States*

Ksenia V. Bets − *Department of Materials Science and NanoEngineering, Rice University, Houston, Texas 77005, United States*

Duy Xuan Luong − *Department of Chemistry, Rice University, Houston, Texas 77005, United States*

Muqing Ren − *Department of Chemistry, Rice University, Houston, Texas 77005, United States*

Michael G. Stanford − *Department of Chemistry, Rice University, Houston, Texas 77005, United States*; orcid.org/0000-0001-9663-1138

Emily A. McHugh − *Department of Chemistry, Rice University, Houston, Texas 77005, United States*

Wala A. Algozeeb − *Department of Chemistry, Rice University, Houston, Texas 77005, United States*

Hua Guo − *Department of Materials Science and NanoEngineering, Rice University, Houston, Texas 77005, United States*

Guanhui Gao − *Department of Materials Science and NanoEngineering, Rice University, Houston, Texas 77005, United States*

Bing Deng − *Department of Chemistry, Rice University, Houston, Texas 77005, United States*

Jinhang Chen − *Department of Chemistry, Rice University, Houston, Texas 77005, United States*

John Tianci Li − *Department of Chemistry and Department of Materials Science and NanoEngineering, Rice University, Houston, Texas 77005, United States*; orcid.org/0000-0002-7218-8298

William T. Carsten − *Department of Chemistry, Rice University, Houston, Texas 77005, United States*

Complete contact information is available at: https://pubs.acs.org/10.1021/acsnano.0c08460

Notes

The authors declare the following competing financial interest(s): Rice University owns intellectual property on the flash Joule heating strategy. J.M.T. is a stockholder in Universal Matter Ltd., the company that licensed the intellectual property from Rice University. J.M.T. is not an officer, director, or employee of Universal Matter Ltd. All conflicts of interest are managed through regular disclosure to the Rice University Office of Sponsored Programs and Research Compliance.

ACKNOWLEDGMENTS

The funding of the research is provided by Air Force Office of Scientific Research (FA9550-19-1-0296) and the DOE-NETL (DE-FE0031794). The authors acknowledge the use of Electron Microscopy Center (EMC) at Rice University. The characterization equipment used in this project is from the Shared Equipment Authority (SEA) at Rice University. Theory

and computations work, by K.V.B. and B.I.Y., was supported by the Department of Energy, BES (DE-SC0012547). W.C. thanks Zhihua Cheng for providing graphite rod counter electrodes and glassy carbon electrodes for the experiments.

REFERENCES

(1) Zhang, T.; Jiang, B.; Xu, Z.; Mendes, R. G.; Xiao, Y.; Chen, L.; Fang, L.; Gemming, T.; Chen, S.; Rummeli, M. H.; Fu, L. Twinned Growth Behaviour of Two-Dimensional Materials. *Nat. Commun.* **2016**, *7*, 13911.

(2) Chhowalla, M.; Shin, H. S.; Eda, G.; Li, L.-J.; Loh, K. P.; Zhang, H. The Chemistry of Two-Dimensional Layered Transition Metal Dichalcogenide Nanosheets. *Nat. Chem.* **2013**, *5*, 263−275.

(3) Xu, D.; Chen, W.; Zeng, M.; Xue, H.; Chen, Y.; Sang, X.; Xiao, Y.; Zhang, T.; Unocic, R. R.; Xiao, K.; Fu, L. Crystal-Field Tuning of Photoluminescence in Two-Dimensional Materials with Embedded Lanthanide Ions. *Angew. Chem., Int. Ed.* **2018**, *57*, 755−759.

(4) Acerce, M.; Voiry, D.; Chhowalla, M. Metallic 1T Phase MoS_2 Nanosheets as Supercapacitor Electrode Materials. *Nat. Nanotechnol.* **2015**, *10*, 313−318.

(5) Chen, W.; Salvatierra, R. V.; Ren, M.; Chen, J.; Stanford, M. G.; Tour, J. M. Laser-Induced Silicon Oxide for Anode-Free Lithium Metal Batteries. *Adv. Mater.* **2020**, *32*, 2002850.

(6) Liu, Q.; Fang, Q.; Chu, W.; Wan, Y.; Li, X.; Xu, W.; Habib, M.; Tao, S.; Zhou, Y.; Liu, D.; Xiang, T.; Khalil, A.; Wu, X.; Chhowalla, M.; Ajayan, P. M.; Song, L. Electron-Doped 1T-MoS_2 *via* Interface Engineering for Enhanced Electrocatalytic Hydrogen Evolution. *Chem. Mater.* **2017**, *29*, 4738−4744.

(7) Xu, H.; Han, D.; Bao, Y.; Cheng, F.; Ding, Z.; Tan, S. J. R.; Loh, K. P. Observation of Gap Opening in 1T' Phase MoS_2 Nanocrystals. *Nano Lett.* **2018**, *18*, 5085−5090.

(8) Yu, Y.; Nam, G.-H.; He, Q.; Wu, X.-J.; Zhang, K.; Yang, Z.; Chen, J.; Ma, Q.; Zhao, M.; Liu, Z.; Ran, F.-R.; Wang, X.; Li, H.; Huang, X.; Li, B.; Xiong, Q.; Zhang, Q.; Liu, Z.; Gu, L.; Du, Y.; et al. High Phase-Purity 1T'-MoS_2- and 1T'-$MoSe_2$-Layered Crystals. *Nat. Chem.* **2018**, *10*, 638−643.

(9) Guo, C.; Pan, J.; Li, H.; Lin, T.; Liu, P.; Song, C.; Wang, D.; Mu, G.; Lai, X.; Zhang, H.; Zhou, W.; Chen, M.; Huang, F. Observation of Superconductivity in 1T'-MoS_2 Nanosheets. *J. Mater. Chem. C* **2017**, *5*, 10855−10860.

(10) Shi, S.; Gao, D.; Xia, B.; Liu, P.; Xue, D. Enhanced Hydrogen Evolution Catalysis in MoS_2 Nanosheets by Incorporation of A Metal Phase. *J. Mater. Chem. A* **2015**, *3*, 24414−24421.

(11) Duerloo, K. A.; Li, Y.; Reed, E. J. Structural Phase Transitions in Two-Dimensional Mo- and W-Dichalcogenide Monolayers. *Nat. Commun.* **2014**, *5*, 4214.

(12) Hong, J.; Hu, Z.; Probert, M.; Li, K.; Lv, D.; Yang, X.; Gu, L.; Mao, N.; Feng, Q.; Xie, L.; Zhang, J.; Wu, D.; Zhang, Z.; Jin, C.; Ji, W.; Zhang, X.; Yuan, J.; Zhang, Z. Exploring Atomic Defects in Molybdenum Disulphide Monolayers. *Nat. Commun.* **2015**, *6*, 6293.

(13) Chang, K.; Hai, X.; Pang, H.; Zhang, H.; Shi, L.; Liu, G.; Liu, H.; Zhao, G.; Li, M.; Ye, J. Targeted Synthesis of 2H- and 1T-Phase MoS_2 Monolayers for Catalytic Hydrogen Evolution. *Adv. Mater.* **2016**, *28*, 10033−10041.

(14) Zhu, J.; Wang, Z.; Yu, H.; Li, N.; Zhang, J.; Meng, J.; Liao, M.; Zhao, J.; Lu, X.; Du, L.; Yang, R.; Shi, D.; Jiang, Y.; Zhang, G. Argon Plasma Induced Phase Transition in Monolayer MoS_2. *J. Am. Chem. Soc.* **2017**, *139*, 10216−10219.

(15) Wang, D.; Zhang, X.; Bao, S.; Zhang, Z.; Fei, H.; Wu, Z. Phase Engineering of A Multiphasic 1T/2H MoS_2 Catalyst for Highly Efficient Hydrogen Evolution. *J. Mater. Chem. A* **2017**, *5*, 2681−2688.

(16) Xiao, J.; Choi, D.; Cosimbescu, L.; Koech, P.; Liu, J.; Lemmon, J. P. Exfoliated MoS_2 Nanocomposite as an Anode Material for Lithium Ion Batteries. *Chem. Mater.* **2010**, *22*, 4522−4524.

(17) Ding, W.; Hu, L.; Dai, J.; Tang, X.; Wei, R.; Sheng, Z.; Liang, C.; Shao, D.; Song, W.; Liu, Q.; Chen, M.; Zhu, X.; Chou, S.; Zhu, X.; Chen, Q.; Sun, Y.; Dou, S. Highly Ambient-Stable 1T-MoS_2 and 1T-WS_2 by Hydrothermal Synthesis under High Magnetic Fields. *ACS Nano* **2019**, *13*, 1694−1702.

(18) Lukowski, M. A.; Daniel, A. S.; Meng, F.; Forticaux, A.; Li, L.; Jin, S. Enhanced Hydrogen Evolution Catalysis from Chemically Exfoliated Metallic MoS_2 Nanosheets. *J. Am. Chem. Soc.* **2013**, *135*, 10274−10277.

(19) Eda, G.; Fujita, T.; Yamaguchi, H.; Voiry, D.; Chen, M.; Chhowalla, M. Coherent Atomic and Electronic Heterostructures of Single-Layer MoS_2. *ACS Nano* **2012**, *6*, 7311−7317.

(20) Guo, Y.; Sun, D.; Ouyang, B.; Raja, A.; Song, J.; Heinz, T. F.; Brus, L. E. Probing the Dynamics of the Metallic-to-Semiconducting Structural Phase Transformation in MoS_2 Crystals. *Nano Lett.* **2015**, *15*, 5081−5088.

(21) Wang, L.; Xu, Z.; Wang, W.; Bai, X. Atomic Mechanism of Dynamic Electrochemical Lithiation Processes of MoS_2 Nanosheets. *J. Am. Chem. Soc.* **2014**, *136*, 6693−6697.

(22) Wu, Z.; Tang, C.; Zhou, P.; Liu, Z.; Xu, Y.; Wang, D.; Fang, B. Enhanced Hydrogen Evolution Catalysis from Osmotically Swollen Ammoniated MoS_2. *J. Mater. Chem. A* **2015**, *3*, 13050−13056.

(23) Cho, S.; Kim, S.; Kim, J. H.; Zhao, X.; Seok, J.; Keum, D. H.; Baik, J.; Choe, D.; Chang, K. J.; Suenaga, K.; Kim, S. W.; Lee, Y. H.; Yang, H. Phase Patterning for Ohmic Homojunction Contact in $MoTe_2$. *Science* **2015**, *349*, 625−628.

(24) Luong, D. X.; Bets, K. V.; Algozeeb, W. A.; Stanford, M. G.; Kittrell, C.; Chen, W.; Salvatierra, R. V.; Ren, M.; McHugh, E. A.; Advincula, P. A.; Wang, Z.; Bhatt, M.; Guo, H.; Mancevski, V.; Shahsavari, R.; Yakobson, B. I.; Tour, J. M. Gram-Scale Bottom-Up Flash Graphene Synthesis. *Nature* **2020**, *577*, 647−651.

(25) Yao, Y.; Huang, Z.; Xie, P.; Lacey, S. D.; Jacob, R. J.; Xie, H.; Chen, F.; Nie, A.; Pu, T.; Rehwoldt, M.; Yu, D.; Zachariah, M. R.; Wang, C.; Yassar, R. S.; Li, J.; Hu, L. Carbothermal Shock Synthesis of High-Entropy-Alloy Nanoparticles. *Science* **2018**, *359*, 1489−1494.

(26) Wang, C.; Ping, W.; Bai, Q.; Cui, H.; Hensleigh, R.; Wang, R.; Brozena, A. H.; Xu, Z.; Dai, J.; Pei, Y.; Zheng, C.; Pastel, G.; Gao, J.; Wang, X.; Wang, H.; Zhao, J.-C.; Yang, B.; Zheng, X.; Luo, J.; Mo, Y.; et al.et al A General Method to Synthesize and Sinter Bulk Ceramics in Seconds. *Science* **2020**, *368*, 521−526.

(27) Yao, Y.; Huang, Z.; Xie, P.; Wu, L.; Ma, L.; Li, T.; Pang, Z.; Jiao, M.; Liang, Z.; Gao, J.; He, Y.; Kline, D. J.; Zachariah, M. R.; Wang, C.; Lu, J.; Wu, T.; Li, T.; Wang, C.; Yassar, R. S.; Hu, L. High Temperature Shockwave Stabilized Single Atoms. *Nat. Nanotechnol.* **2019**, *14*, 851−857.

(28) Stanford, M. G.; Bets, K. V.; Luong, D. X.; Advincula, P. A.; Chen, W.; Li, J. T.; Wang, Z.; McHugh, E. A.; Algozeeb, W. A.; Yakobson, B. I.; Tour, J. M. Flash Graphene Morphologies. *ACS Nano* **2020**, *14*, 13691−13699.

(29) Algozeeb, W. A.; Savas, P. E.; Luong, D. X.; Chen, W.; Kittrell, C.; Bhat, M.; Shahsavari, R.; Tour, J. M. Flash Graphene from Plastic Waste. *ACS Nano* **2020**, *14*, 15595−15604.

(30) Wang, X.; Shen, X.; Wang, Z.; Yu, R.; Chen, L. Atomic-Scale Clarification of Structural Transition of MoS_2 Upon Sodium Intercalation. *ACS Nano* **2014**, *8*, 11394−11400.

(31) Wypych, F.; Solenthaler, C.; Prins, R.; Weber, T. Electron Diffraction Study of Intercalation Compounds Derived from 1T-MoS_2. *J. Solid State Chem.* **1999**, *144*, 430−436.

(32) Sharma, C. H.; Surendran, A. P.; Varghese, A.; Thalakulam, M. Stable and Scalable 1T MoS_2 with Low Temperature-Coefficient of Resistance. *Sci. Rep.* **2018**, *8*, 12463.

(33) Zhang, Y.; Mu, Z.; Yang, C.; Xu, Z.; Zhang, S.; Zhang, X.; Li, Y.; Lai, J.; Sun, Z.; Yang, Y.; Chao, Y.; Li, C.; Ge, X.; Yang, W.; Guo, S. Rational Design of MXene/1T-2H MoS_2-C Nanohybrids for High-Performance Lithium-Sulfur Batteries. *Adv. Funct. Mater.* **2018**, *28*, 1707578.

(34) Peng, J.; Liu, Y.; Luo, X.; Wu, J.; Lin, Y.; Guo, Y.; Zhao, J.; Wu, X.; Wu, C.; Xie, Y. High Phase Purity of Large-Sized 1T'-MoS_2 Monolayers with 2D Superconductivity. *Adv. Mater.* **2019**, *31*, No. e1900568.

https://dx.doi.org/10.1021/acsnano.0c08460
ACS Nano 2021, 15, 1282−1290

(35) Xiao, Y.; Zhou, M.; Liu, J.; Xu, J.; Fu, L. Phase Engineering of Two-Dimensional Transition Metal Dichalcogenides. *Sci. China Mater.* **2019**, *62*, 759−775.
(36) Fan, X.; Xu, P.; Zhou, D.; Sun, Y.; Li, Y. C.; Nguyen, M. T.; Terrones, M.; Mallouk, T. E. Fast and Efficient Preparation of Exfoliated 2H MoS_2 Nanosheets by Sonication-Assisted Lithium Intercalation and Infrared Laser-Induced 1T to 2H Phase Reversion. *Nano Lett.* **2015**, *15*, 5956−5960.
(37) Lin, Y.-C.; Dumcenco, D. O.; Huang, Y.-S.; Suenaga, K. Atomic Mechanism of the Semiconducting-to-Metallicphase Transition in Single-Layered MoS_2. *Nat. Nanotechnol.* **2014**, *9*, 391−396.
(38) Jin, Q.; Liu, N.; Chen, B.; Mei, D. Mechanisms of Semiconducting 2H to Metallic 1T Phase Transition in Two-Dimensional MoS_2 Nanosheets. *J. Phys. Chem. C* **2018**, *122*, 28215−28224.
(39) Tan, S. J. R.; Sarkar, S.; Zhao, X.; Luo, X.; Luo, Y. Z.; Poh, S. M.; Abdelwahab, I.; Zhou, W.; Venkatesan, T.; Chen, W.; Quek, S. Y.; Loh, K. P. Temperature- and Phase-Dependent Phonon Renormalization in 1T'-MoS_2. *ACS Nano* **2018**, *12*, 5051−5058.
(40) Liu, Z.; Li, N.; Su, C.; Zhao, H.; Xu, L.; Yin, Z.; Li, J.; Du, Y. Colloidal Synthesis of 1T' Phase Dominated WS_2 towards Endurable Electrocatalysis. *Nano Energy* **2018**, *50*, 176−181.
(41) Liu, Q.; Li, X.; Xiao, Z.; Zhou, Y.; Chen, H.; Khalil, A.; Xiang, T.; Xu, J.; Chu, W.; Wu, X.; Yang, J.; Wang, C.; Xiong, Y.; Jin, C.; Ajayan, P. M.; Song, L. Stable Metallic 1T-WS_2 Nanoribbons Intercalated with Ammonia Ions: The Correlation between Structure and Electrical/Optical Properties. *Adv. Mater.* **2015**, *27*, 4837−4844.
(42) Gao, G.; Jiao, Y.; Ma, F.; Jiao, Y.; Waclawik, E.; Du, A. Charge Mediated Semiconducting-to-Metallic Phase Transition in Molybdenum Disulfide Monolayer and Hydrogen Evolution Reaction in New 1T' Phase. *J. Phys. Chem. C* **2015**, *119*, 13124−13128.
(43) Zhou, X.; Shu, H.; Li, Q.; Liang, P.; Cao, D.; Chen, X. Electron-Injection Driven Phase Transition in Two-Dimensional Transition metal dichalcogenides. *J. Mater. Chem. C* **2020**, *8*, 4432−4440.
(44) Wang, S.; Zhang, D.; Li, B.; Zhang, C.; Du, Z.; Yin, H.; Bi, X.; Yang, S. Ultrastable In-Plane 1T−2H MoS_2 Heterostructures for Enhanced Hydrogen Evolution Reaction. *Adv. Energy Mater.* **2018**, *8*, 1801345.

https://dx.doi.org/10.1021/acsnano.0c08460
ACS Nano 2021, 15, 1282−1290